Universiteit
Antwerpen

This item is the archived peer-reviewed author-version of:

Atom counting from a combination of two ADF STEM images

Reference:
Sentürk Duygu Gizem, Yu C.P., De Backer A., Van Aert Sandra.- Atom counting from a combination of two ADF STEM images
Ultramicroscopy - ISSN 1879-2723 - 255(2024), 113859
Full text (Publisher's DOI): https://doi.org/10.1016/J.ULTRAMIC.2023.113859
To cite this reference: https://hdl.handle.net/10067/2010080151162165141

uantwerpen.be
Institutional repository IRUA

Atom counting from a combination of two ADF STEM images

D.G. Şentürk[a,b], C.P. Yu[a,b], A. De Backer[a,b], S. Van Aert[a,b]

[a] *Electron Microscopy for Materials Science (EMAT), University of Antwerp, Groenenborgerlaan 171, 2020 Antwerp, Belgium*
[b] *NANOlab Center of Excellence, University of Antwerp, Groenenborgerlaan 171, 2020 Antwerp, Belgium*

Abstract

To understand the structure-property relationship of nanostructures, reliably quantifying parameters, such as the number of atoms, is important. Advanced statistical methodologies have made it possible to count the number of atoms for monotype crystalline nanoparticles from a single ADF STEM image. Recent developments enable one to simultaneously acquire multiple ADF STEM images. Here, we present an extended statistics-based method for atom counting from a combination of multiple statistically independent ADF STEM images which improves the accuracy and allows one to retrieve precise atom-counts, especially for images acquired with lower electron doses and multiple element structures.

1. Introduction

Nanoparticles have been the focus of many research studies due to their unique properties and potential applications in various fields. The physical properties of nanomaterials such as their electronic, optical, magnetic, and mechanical properties are highly dependent on the size, shape, chemical composition, and structure. Therefore, understanding the relationship between the structure and properties is crucial for designing and optimizing their performance for specific applications. For this purpose, aberration-corrected scanning transmission electron microscopy (STEM) has emerged as a powerful tool for the characterization of nanostructures.

The STEM technique provides different imaging modes based on the size of the inner and outer angles of the annular detector [1, 2]. High-angle annular dark-field (HAADF) STEM imaging is one of the most popular modes since it provides Z-contrast and thickness contrast in the images. Over the past years, many quantification procedures have been developed to determine thickness or composition from HAADF STEM images. One valuable quantification procedure is atom counting [3–6], which reveals the number of atoms at each atomic column. These atom-counts can even be used to construct a three-dimensional (3D) atomic model based on a single 2D STEM image [7–10]. This analysis is for example important when studying catalysts, where the surface morphology is crucial for their applications.

To perform atom counting, both simulations- and statistics-based methods have been proposed [3, 11, 12]. The statistics-based methodology introduced by Van Aert et al. [4], is advantageous as it enables atom counting without requiring any prior information about the structure from simulations. The so-called scattering cross-section (SCS) is used as a measurement in this method, which is defined as the total intensity of electrons of each atomic column scattered toward the ADF detector [13, 14]. This measurement is advantageous for the quantitative interpretation of HAADF STEM images since it is sensitive to the number and type of atoms while it is robust to experimental parameters such as defocus, source size broadening, and slight sample mistilt [15, 16]. The scattering cross-section can be computed either by using Voronoi cells [8, 17] or by estimating the volume of Gaussian functions which are fitted to the atomic columns in the image [5, 12, 13, 18]. The traditional statistics-based method which is introduced for the analysis of a single ADF STEM image is very reliable and provides atom counts with single atom sensitivity if the signal-to-noise ratio in the underlying images is sufficiently large [12]. The capabilities and inherent limitations of the methodology when investigating images acquired under low electron dose conditions or for small nanoparticles are discussed in [5, 19].

In the past, HAADF STEM imaging with its incoherent nature has often been considered to be the best detector setting for quantification purposes due to its direct interpretability [3, 11, 12, 20, 21]. However, other annular detector geometries possess unique strengths. For example, low-angle annular dark-field (LAADF) and medium-angle annular dark-field (MAADF) STEM images provide valuable information due to the larger amount of electrons collected in this region. For example, it has been demonstrated that, despite the higher contribution of coherent scattering, LAADF and MAADF imaging are optimal for counting the number of atoms in relatively thin mono-atomic samples [18]. Our recent study suggested that the combination of scattering cross-sections originating from multiple ADF STEM detector regions is advantageous when unscrambling the number of atoms and type of elements in heterogeneous nanostructures [22]. When the detector regions have a different scattering behaviour, they have independent composition and thickness information. With the development of pixelated direct electron detectors, the 4D STEM technique enables reconstructing these multiple STEM images belonging to arbitrary annular detector regions without the need for preconfigured instrumental settings [23].

Therefore, in this study, we extend the statistical atom-counting procedure enabling the analysis of multiple scattering cross-

sections signals. Apart from the expected advantage for quantifying heterogeneous materials, this approach is envisaged to be beneficial under lower dose conditions in the case of monoatomic nanocrystals. Within the traditional statistical approach introduced for a single STEM image, the distribution of scattering cross-sections is modelled by a one-dimensional Gaussian mixture model (1D GMM). This Gaussian mixture model is a probabilistic distribution model which assumes that the dataset under investigation is generated as a statistical random draw from a mixture of normal distributions. By estimating the parameters of the mixture model, one can decompose the dataset, i.e. the distribution of scattering cross-sections, into overlapping normal distributions [24]. This approach is widely used in various applications such as pattern recognition, clustering, image segmentation and is also the main procedure of the statistical atom-counting method. When two statistically independent sets of scattering cross-sections from multiple images are available, a multivariate approach is required. Therefore, in this study a two-dimensional Gaussian mixture model (2D GMM) is explored for the classification of the two-dimensional distribution of the scattering cross-sections for atom counting.
The organisation of the paper is as follows. In Section 2, the two-dimensional Gaussian mixture model will be described in terms of atom counting. In Section 3, the methodology will be applied to a simulated spherical Ni nanoparticle and the performance of the methodology will be presented by comparing the estimated atom counts with the traditional statistical atom-counting procedure based on the one-dimensional Gaussian mixture model. Then, in Section 4, the advantages and limitations of the methodology will be discussed. In Section 5, the prospects of the methodology for multiple element nanostructures will be presented. Finally, in Section 6 conclusions will be drawn.

2. Methodology

The traditional statistical atom-counting procedure using a single ADF STEM image consists of two steps [12]. In the first step, an experimental image is described as a superposition of Gaussian functions which are peaked at the atomic column positions. The unknown parameters of this model are estimated by minimising the least squares criterion. From the estimated parameters, the volume under each Gaussian function is determined, corresponding to the so-called scattering cross-section for each projected atomic column [5, 13]. In the second step, the estimated scattering cross-sections serve as an input for a Gaussian mixture model (GMM) analysis combined with the use of an order selection criterion. This second step will be extended here from 1D to 2D and will be explained in detail in this section.

2.1. Probability distribution of the 2D scattering cross-sections

The estimated scattering cross-sections obtained from a single ADF STEM image, denoted as $SCS_{1,n}$ with n the atomic column index, can be visualised in a one-dimensional histogram as shown in Fig. 1(a) which is generated based on a simulated Au nanoparticle. Similarly, if a combination of two ADF STEM images is considered, the scattering cross-sections extracted from both images, i.e. $SCS_{1,n}$ and $SCS_{2,n}$, can be visualised in a 2D distribution plot as illustrated in Fig. 1(b). In analogy to the 1D case, the 2D dataset ideally consists of individual components where each component corresponds to a set of atomic columns with the same number of atoms located on top of each other for monotype nanostructures or to a set of atomic columns with the same number of atoms of each atom type for heterostructures consisting of a mixture of elements. As demonstrated in Fig. 1, the components are smeared out due to the presence of unavoidable experimental noise. Therefore, the estimated scattering cross-sections fluctuate around their expectation values causing a smearing effect of the components. This complicates the assignment of the number of atoms in each atomic column by means of visual inspection only. One method for solving this problem is to consider the estimated scattering cross-sections as independent statistical draws from an unknown probability distribution. For a 1D dataset, a univariate GMM consisting of a superposition of 1D normal components has been shown to work. For a 2D dataset, this model will be extended to a multivariate GMM consisting of a superposition of 2D normal components describing the probability of observing a particular combination of scattering cross-section values resulting from the two images. From the observed scattering cross-section values, the parameters of this 2D GMM including the locations, widths, and the number of components will be estimated. Once the 2D GMM is known, the number of atoms per atomic column can be identified by assigning the pair of scattering cross-sections to the component of the estimated probability distribution with the highest probability of generating this pair [5, 12].
The probability density function of a 2D GMM with G components can be written as

$$f_{\text{mix}}\left(\mathbf{SCS}_n;\mathbf{\Psi}_G\right) = \sum_{g=1}^{G} \pi_g \mathcal{N}\left(\mathbf{SCS}_n;\boldsymbol{\mu}_g,\Sigma_g\right), \quad (1)$$

with $\mathbf{SCS}_n = \left(SCS_{1,n}, SCS_{2,n}\right)^T$ the 2D stochastic variable for the scattering cross-sections of the nth atomic column corresponding to the two detector regions. The 2D normal distribution function $\mathcal{N}\left(\mathbf{SCS}_n;\boldsymbol{\mu}_g,\Sigma_g\right)$ is generated by atomic columns having the same number of atoms and composition and can be described as [4, 12, 24]:

$$\mathcal{N}\left(\mathbf{SCS}_n;\boldsymbol{\mu}_g,\Sigma_g\right) = \frac{1}{2\pi\sqrt{\det\left(\Sigma_g\right)}} \exp\left(-\frac{1}{2}(\mathbf{SCS}_n-\boldsymbol{\mu}_g)^T\Sigma_g^{-1}(\mathbf{SCS}_n-\boldsymbol{\mu}_g)\right) \quad (2)$$

with $\boldsymbol{\mu}_g = \left(\mu_{1,g},\mu_{2,g}\right)^T$ the 2D location vector of the gth component. The covariance matrix, Σ_g, is given by:

$$\Sigma_g = \begin{pmatrix} \sigma_{1,g}^2 & 0 \\ 0 & \sigma_{2,g}^2 \end{pmatrix} \quad (3)$$

with $\sigma_{1,g}$ and $\sigma_{2,g}$ the width of the gth normal component corresponding to the two detector regions, respectively. These effective widths $\sigma_{1,g}$ and $\sigma_{2,g}$ of the components can be described

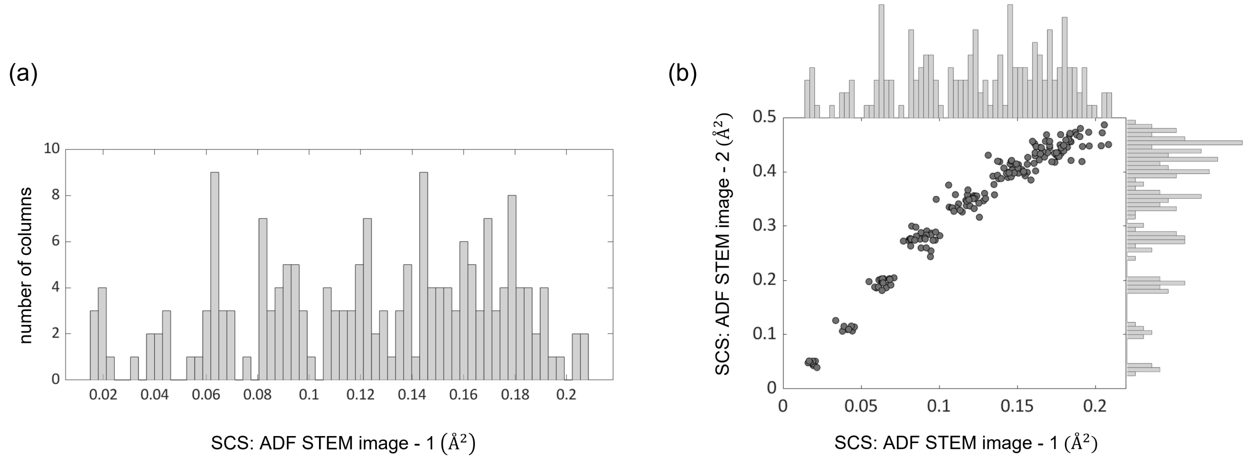

Figure 1: Example of (a) the distribution of the scattering cross-sections estimated from a single ADF STEM image in the form of a 1D histogram and (b) a 2D distribution of scattering cross-sections estimated from two ADF STEM images represented in a scatter plot together with the 1D histograms of each dataset projected along the x- and y-direction.

as [10, 25]:

$$\sigma_{1,g} = \sqrt{\sigma^2_{1,di} + \frac{\mu_{1,g}}{d}} \tag{4}$$

and

$$\sigma_{2,g} = \sqrt{\sigma^2_{2,di} + \frac{\mu_{2,g}}{d}} \tag{5}$$

with

$$\Sigma_{di} = \begin{pmatrix} \sigma^2_{1,di} & 0 \\ 0 & \sigma^2_{2,di} \end{pmatrix} \tag{6}$$

describing the dose-independent contribution to the component's width along both axes and d the incoming electron dose. The unknown parameters in the mixture model with G components are summarized in the vector $\mathbf{\Psi}_G$:

$$\mathbf{\Psi}_G = (\pi_1, ..., \pi_{G-1}, \mu_{1,1}, ..., \mu_{1,G}, \mu_{2,1}, ...\mu_{2,G}, \Sigma_{di})^T \tag{7}$$

with π_g the mixing proportion of the gth component. Since the mixing proportions sum up to unity, $\sum_{g=1}^{G} \pi_g = 1$, the Gth mixing proportion is omitted in the parameter vector.

2.2. Maximum likelihood estimation

In order to evaluate the unknown parameters of the mixture model, the maximum likelihood estimator is used [24, 26–28]. Estimates are found by maximizing the log-likelihood function of the unknown parameter vector $\mathbf{\Psi}_G$ for a given set of observed scattering cross-sections $\mathbf{S\hat{C}S}_n$, which is defined as

$$\log L(\mathbf{\Psi}_G) = \sum_{n=1}^{N} \log\left(\sum_{g=1}^{G} \pi_g \mathcal{N}\left(\mathbf{S\hat{C}S}_n; \boldsymbol{\mu}_g, \Sigma_g\right)\right). \tag{8}$$

A solution for the parameters $\mathbf{\Psi}_G$ for a fixed number of components G can be found in an iterative manner using the so-called expectation-maximization (EM) algorithm. The algorithm proceeds in two steps: the E-step for expectation and the M-step for maximisation. In practice, starting from an initial set of parameters $\mathbf{\Psi}_G^{(0)}$, the posterior probability that the nth scattering cross section with observed value $\mathbf{S\hat{C}S}_n$ belongs to the gth component of the mixture is calculated in the E-step, i.e.:

$$\tau_g\left(\mathbf{S\hat{C}S}_n; \mathbf{\Psi}_G^{(k)}\right) = \frac{\pi_g^{(k)} \mathcal{N}\left(\mathbf{S\hat{C}S}_n; \boldsymbol{\mu}_g^{(k)}, \Sigma_g^{(k)}\right)}{\sum_{h=1}^{G} \pi_h^{(k)} \mathcal{N}\left(\mathbf{S\hat{C}S}_n; \boldsymbol{\mu}_g^{(k)}, \Sigma_g^{(k)}\right)} \tag{9}$$

for $g = 1, ..., G$ and $n = 1, ..., N$. The iteration step is denoted by k.
The M-step calculates the updated estimate $\mathbf{\Psi}_G^{(k+1)}$. The update formula for the mixing proportions is given by:

$$\pi_g^{(k+1)} = \frac{\sum_{n=1}^{N} \tau_g\left(\mathbf{S\hat{C}S}_n; \mathbf{\Psi}_G^{(k)}\right)}{N} \tag{10}$$

for $g = 1, ..., G$. Updates for the unknown parameters $\boldsymbol{\mu}_g^{(k+1)}$ and $\Sigma_{di}^{(k+1)}$ are given by:

$$\boldsymbol{\mu}_g^{(k+1)} = \frac{\sum_{n=1}^{N} \tau_g\left(\mathbf{S\hat{C}S}_n; \mathbf{\Psi}_G^{(k)}\right) \mathbf{S\hat{C}S}_n}{\sum_{n=1}^{N} \tau_g(\mathbf{S\hat{C}S}_n; \mathbf{\Psi}_G^{(k)})}, \tag{11}$$

$$\Sigma_{di}^{(k+1)} = \frac{\sum_{g=1}^{G}\sum_{n=1}^{N}[\tau_g(\mathbf{SCS}_n;\mathbf{\Psi}_G^{(k)})(\mathbf{SCS}_n-\boldsymbol{\mu}_g^{(k+1)})(\mathbf{SCS}_n-\boldsymbol{\mu}_g^{(k+1)})^T]-\frac{\boldsymbol{\mu}_g^{(k+1)}}{d}}{N} \tag{12}$$

The iterative algorithm continues until convergence of the log-likelihood is achieved based on the difference between consecutive log-likelihood values $\frac{\log L(\mathbf{\Psi}_G^{(k)})-\log L(\mathbf{\Psi}_G^{(k-1)})}{\log L(\mathbf{\Psi}_G^{(k-1)})} < \epsilon$ where $\epsilon > 0$ is the pre-defined tolerance level. The value of the likelihood is improved for every successful iteration of the E- and M-steps.

2.3. Initialisation for the EM algorithm

Although the EM algorithm is a standard tool for maximum-likelihood estimation, the method has some drawbacks such as trapping on a local maximum and slow convergence in some situations. However, it is reported that the performance of the algorithm can be improved by an appropriate choice of initial

values for the parameters [24]. In practice, selecting appropriate starting values for the EM algorithm is often a challenging task requiring prior knowledge of the data and the model parameters. Since the model order G is not known beforehand, GMMs with increasing number of components are estimated, starting from 1 component up to a maximum number of components which will depend on the sample under study. For a 1D GMM, the estimated parameters of the models with order G can typically be used for the model with order $G + 1$. The most efficient starting values, providing unbiased estimates, have been derived in previous studies for the conventional atom-counting procedure which is performed by using the 1D GMM approach based on a set of scattering cross-sections extracted from a single ADF STEM image [5]. For the multivariate approach, the starting values for mixing proportions and covariance matrix can be chosen accordingly

$$\pi_g^{(0)} = \frac{1}{G} \tag{13}$$

$$\Sigma_{i,di}^{(0)} = \frac{\max(SCS_{i,n}) - \min(SCS_{i,n})}{2 \cdot G} \tag{14}$$

where $i = 1, 2$ for the two dimensions. The starting value for the covariance is only used when estimating the GMM with one component. For the models with increasing number of components, i.e. $G + 1$ components, the starting values for $\Sigma_{i,di}^{(0)}$ are equal to the estimated covariance matrix of the model with G components. To define reasonable starting values for the locations of components, various approaches are proposed in the literature [24, 29–33]. In some cases, the selection of random initial locations ranging between the minimum and maximum of the data set is suggested where the algorithm can run multiple times with different starting values to explore the solution space and reach to the global maximum. For a one-dimensional dataset, such a random partitioning approach is proven to be useful. However, when a combination of two sets of scattering cross-sections is investigated, the complexity of the problem increases and different strategies are required. In this study, the so-called *emEM* algorithm that was proposed by Biernacki et al., is implemented [29].

The *emEM* is a stochastic initialization strategy which is based on the idea of running short EM (em) algorithms before a long EM evaluation. In this manner, a rough estimate for the propagation of the component locations is obtained. The algorithm consists of the following steps. First, for a given number of components G, the algorithm is started by selecting G random values from the 2D dataset. Subsequently, the remaining dataset is partitioned into G groups based on the minimum Euclidean distance from each observation $\mathbf{SCS}_n$ to one of the selected G values. The means of the resulting subsets are then assigned as starting locations for the short EM calculation. The short EM algorithm is then run for a few iterations or until some rough convergence criterion is met. Here, the criterion for convergence is defined by a relatively high tolerance value (i.e. $\epsilon = 10^{-2}$ and maximum 100 iterations). This process is repeated several times, here 5 times, to determine the optimal candidate locations in terms of the maximum likelihood. The estimated candidate locations with the best likelihood from the 5 short EM runs are then used as starting values for the main EM algorithm, also known as the long EM. The long EM runs until final convergence is reached by assigning a high number of iterations and a low convergence threshold ϵ (i.e. $\epsilon = 10^{-8}$ and maximum 1000 iterations). This combination of 5 short EM runs and one long EM run is repeated several times, here 40 times. This is also noted as 40emEM. The estimated model parameters for the 2D GMM then correspond to the model maximizing the likelihood. It should be noted that the required number of repetitions for both short and long EM runs to estimate the most accurate component locations would differ depending on the nature of the dataset and the number of Gaussian components in the mixture model.

2.4. *The number of components in the 2D Gaussian mixture model*

The previous paragraphs describe how to estimate the parameters of the 2D GMM with a given number of G components. To determine the order of the mixture model describing the underlying distribution of the scattering cross-sections, the models with different number of components are evaluated using an order selection criterion. For this purpose, the integrated classification likelihood (ICL) criterion is proposed as the optimal methodology for the 1D GMM approach because it outperforms other order-selection criteria [4, 5, 34]. Therefore, in this study, the ICL criterion will be adapted for 2D GMM. The ICL criterion is formulated as

$$ICL(G) = -2\log L(\mathbf{\Psi_G}) + [2EN(\hat{\tau}) + \nu \log N], \tag{15}$$

where the negative log-likelihood term $-2\log L(\mathbf{\Psi}_G)$ measures the model fit and decreases with an increasing number of Gaussian components. The model fit is expected to improve with increasing number of components, as more details in the dataset are described. However, this does not mean that the quality of the model would improve since the details described by the model would be random. Therefore, the term in brackets penalizes the high-order models by measuring the complexity of the model and increases with increasing number of components. The first term $EN(\hat{\tau})$ represents the entropy and the second term consists of the sample size N and the number of parameters ν in the mixture model. The entropy for the model with G components is evaluated by

$$EN(\hat{\tau}) = -\sum_{g=1}^{G}\sum_{n=1}^{N} \tau_g\left(\mathbf{SCS}_n; \mathbf{\Psi}_G\right) \log \tau_g\left(\mathbf{SCS}_n; \mathbf{\Psi}_G\right). \tag{16}$$

The correct number of Gaussian components often corresponds to a local minimum at the evaluated ICL curve as a function of the number of components. Since multiple local minima might be present, a validation step through a comparison with image simulations is often recommended.

3. Atom counting from a combination of ADF STEM images for a Ni nanoparticle

In this section, the atom-counting procedure from a combination of two ADF STEM images is illustrated using a simulated spherical Ni (Z=28) nanoparticle. The input structure

is presented in Fig. 2(a). The thickness of the nanoparticle varies from 1 up to 16 atoms. Two ADF STEM images are reconstructed from a simulated 4D STEM dataset by using the MULTEM software [35]. The parameters of the multislice simulation using the frozen-phonon approximation are listed in Table 1. It should be noted that the contributions from inelastic plasmon excitations are not included in the simulations which would be important for quantitatively matching simulated and experimental intensity values at low scattering angles, especially for thicker samples [36]. The annular detector collection regions of the virtual ADF STEM images are chosen as 21-40 mrad and 40-170 mrad based on the optimal experiment design [22]. Details of this analysis are provided in Appendix A. In this section, these images will be referred as 'Image-1' and 'Image-2' respectively. The images are convolved with a Gaussian function with a given FWHM to account for source size broadening. The two reconstructed ADF STEM images for an incident electron dose of $10^4 e^-/\text{Å}^2$ are shown in Fig. 2(b)-(c), respectively. The simulated images are fitted by a superposition of Gaussian peaks and the scattering cross-section values are measured from the volume under each Gaussian peak [37]. Additionally, the effect of scan distortion is introduced to the measured scattering cross-sections as a normal distribution with zero mean and standard deviations equal to $\sigma_{1,di} = 0.0047$ and $\sigma_{2,di} = 0.0016$ for Image-1 and Image-2.

Parameter	Value
Zone axis orientation	[100]
Acceleration voltage	120 kV
Defocus	-17.184 Å
Spherical aberration	0.001 mm
Semi-convergence angle	20 mrad
Real space probe sampling distance	0.15 Å
Number of pixels in real space ($K \times L$)	368×368
Pixel size in reciprocal space	0.0137 Å^{-1}
Number of pixels in reciprocal space ($M \times N$)	882×882
Maximal outer detector angle	170 mrad
Debye-Waller B factor Ni	0.3783 Å^2
FWHM of the source image	0.7 Å

Table 1: Settings used for the Ni nanoparticle multislice simulations with the MULTEM software.

The two sets of scattering cross-sections are presented as a 2D distribution plot in Fig. 2(d). The associated 1D histograms of the scattering cross-sections for each ADF STEM image are represented by the projections of the 2D dataset along the x- and y-axis of the figure. It is important to note that only the scattering cross-sections from the 40-170 mrad detector region exhibit a monotonically increasing behaviour with thickness. This behaviour is usually exploited in order to assign the number of atoms to the clustered scattering cross-section. For the 21-40 mrad detector a non-monotonic increase is observed which is attributed to the coherent contributions becoming dominant in this regime.

Based on the set of scattering cross-section values, the number of components and the parameters of the 2D Gaussian mixture model are estimated. Fig. 2(e) compares three ICL curves to assess the number of components in the GMM. The ICL curves correspond to the evaluation of the individual ADF STEM images using a 1D GMM and the combination of images using a 2D GMM. The correct number of components G is equal to 16 and is marked by the grey dashed line along the three curves. The blue and orange curves demonstrate that the information from the single images is insufficient for determining the correct number of components, whereas the yellow curve, with a minimum at $G = 16$ components, shows that the combination of two images can enhance the performance of the order selection criterion. Fig. 2(d) displays the estimated probability distribution using 16 Gaussian components describing the observations for scattering cross-sections. The projections of the estimated 2D probability distribution are shown onto the 1D histograms by the Gaussian components with solid lines. For 21-40 mrad it is impossible to decompose the dataset correctly due to the highly overlapping components. Also for the 40-170 mrad detector, it is likely to underestimate the number of components due to the higher overlap of the Gaussian components for larger scattering cross-sections. In this example, the combination of the two datasets helps to identify the correct number of Gaussian components as the overlap between different components is reduced in the 2D scatter plot.

From the estimated 2D GMM, the number of atoms can be counted from 1 to the number of estimated Gaussian components in Fig. 2 (d). For this purpose, the monotonic increase of the scattering cross-sections along the axis corresponding to 40-170 mrad detector can be used. The number of atoms for each atomic column is determined by assigning each scattering cross-section to the component of the estimated probability distribution with the highest probability for that scattering cross-section. In Fig. 2(f)-(h) the difference between the true and the estimated atom counts is shown for the information obtained from Image-1, Image-2 and the combination of both images, respectively. The atom-counting error is significantly reduced by using the information from the two images, resulting in a correct estimation of the number of atoms for 90% of the atomic columns. On the other hand, for the individual images only 29% of the atomic columns in Fig. 2(f) and 70% of the atomic columns in Fig. 2(g) could be counted correctly.

4. Possibilities and limitations

In this section, we present an evaluation of the atom-counting performance using a combination of two ADF STEM images with a 2D GMM procedure in comparison to the 1D GMM approach based on measurements from a single ADF STEM image. The accuracy of the atom-counting results highly depends on the estimation of the correct number of components using the ICL. Thus, determining the limiting factors to obtain the correct number of components is of high relevance. Here, we explore the two dominant factors that affect the accuracy of atom counting: the number of observations and the amount

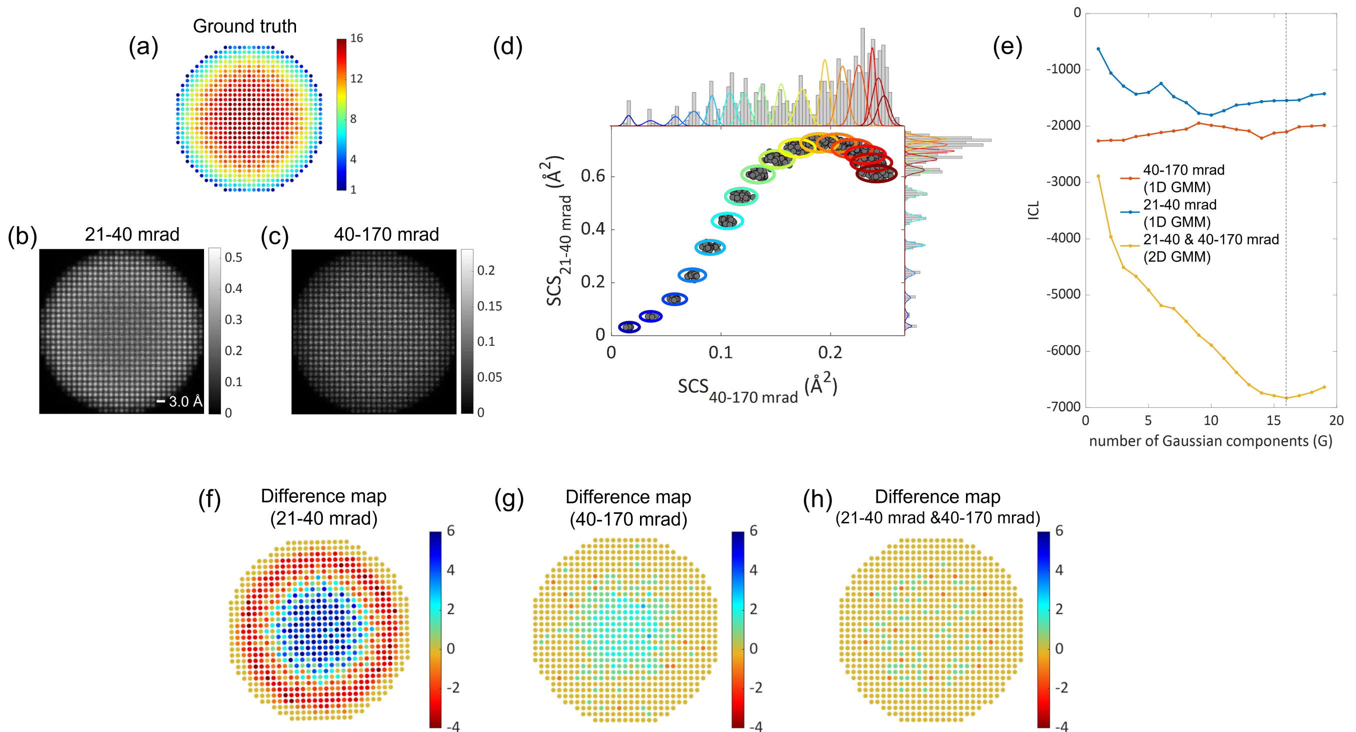

Figure 2: (a) Input structure for a simulated Ni nanoparticle with thickness up to 16 atoms. (b) ADF STEM image of a Ni nanoparticle with 21-40 mrad (Image-1) and (c) 40-170 mrad (Image-2) detector collection region for an electron dose of $10^4 e^-/A^2$. (d) The 2D distribution of the scattering cross-sections together with the estimated 2D GMM. The projections of the 2D GMM onto the 1D histograms of the scattering cross-sections extracted from Image-1 and Image-2 are displayed with the solid lines. (e) The ICL evaluation from each single dataset (blue and orange curves) and from the combination of the two datasets (yellow curve). (f) The difference between the input and the estimated atom-counting results from Image-1 (21-40 mrad), (g) Image-2 (40-170 mrad), and (h) the combination of the two images for an incident electron dose of $10^4 e^-/A^2$.

of overlap of the components in the GMM. The latter can be directly related to the presence of (electron counting) noise in experiments.

First, the average number of observations per Gaussian component in the GMM needed to obtain reliable results from the evaluation of the ICL is derived as a function of the average relative width of the Gaussian components. This relative width is a critical parameter that strongly affects the performance of the ICL evaluation. When investigating a single ADF STEM image, the relative width in a 1D GMM is defined as the ratio of the average width of the Gaussian components to the average increment between successive components, i.e. the σ/δ-ratio. This ratio determines the degree of separation between the Gaussian components. From a physical point of view, a higher overlap of components corresponds to imaging conditions with a low signal-to-noise ratio which decreases the accuracy of ICL evaluation. For the case of scattering cross-section values corresponding to two detector regions, a σ/δ-ratio can now be defined for both axes as illustrated in Fig. 3(a). The statistical draw in this figure originates from a 2D probability distribution with 10 components corresponding to the scattering cross-section values of a Ni column in a unit cell with 1 up to 10 atoms for collection angles 21-40 mrad and 40-170 mrad. The number of observations is equal to 50 for each component. The relative width of the components equals 0.16 for both axes, denoted as $\Sigma/\Delta = 0.16$. This small relative width would correspond to high-dose imaging conditions resulting in perfectly distinguishable components. For this example, the reliability of the ICL as a function of the relative width, varying from 0.1 to 0.3, is evaluated. This example allows for a simple interpretation of the average relative width, which is the same for the two axes, and allows for a fair comparison of the performance of the 2D GMM with respect to the 1D GMM. The necessary number of observations per component N/G to achieve a percentage of 95% of correctly assigned number of components are presented in Fig. 3(b) for the 2D GMM and the 1D GMM based on the 40-170 mrad detector. For both cases, it is observed that the required number of observations increases with the relative width. However, for higher relative widths, the combination of two images can provide a high percentage of correctly assigned number of components for a limited number of observations. This result illustrates the benefit of the extension of the statistics-based atom-counting method to two dimensions, for a small nanoparticle with a limited number of atomic columns (i.e. small N/G) imaged at low dose conditions (i.e. high relative width).

Next, the performance of the ICL is investigated as a function of the incident electron dose and for a higher number of

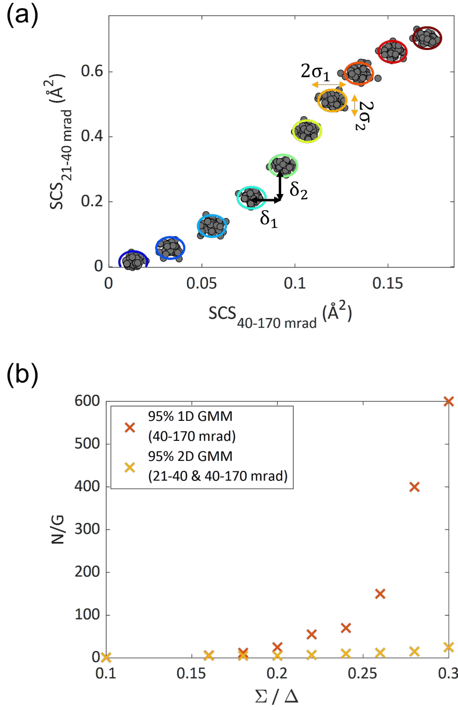

Figure 3: (a) Estimated 2D GMM generated with $N/G = 50$ observations, $G = 10$ components, and $\Sigma/\Delta = 0.16$. σ_i and δ_i are illustrated for both axes. (b) The average number of observations per component N/G required to achieve 95% correctly identified number of components as a function of the relative width Σ/Δ.

components, i.e. up to 30 atoms thickness. In this case the scattering cross-sections corresponding to the 21-40 mrad detector show a non-monotonic behaviour. In Fig. 4(a), the impact of Poisson noise on the two ADF STEM images is demonstrated for two different incident electron doses ($N_d = 10^5 e^-/\text{Å}^2$ and $N_d = 10^4 e^-/\text{Å}^2$). In Fig. 4(b) the distribution of scattering cross-sections obtained from the combination of ADF STEM images under both conditions is displayed along with the estimated 2D GMM. For both datasets the number of observations per thickness value equals $N/G = 15$. From the scatter plots, it is clear that the dataset corresponding to the higher dose ($N_d = 10^5 e^-/\text{Å}^2$), with well separated components, enables a more accurate estimation of the number of components as compared to the lower dose ($N_d = 10^4 e^-/\text{Å}^2$). The overlap of the components at the lower dose will challenge the correct determination of the number of components and therefore also the assignment of the correct number of atoms. In Fig. 4(c) the fraction of correctly identified number of components from the ICL is presented as a function of electron dose. To do that, 100 noise realisations are generated for both datasets under different electron dose conditions. The blue and orange curves are obtained from the ICL evaluation for single ADF STEM measurements using a 1D GMM while the yellow curve is calculated based on the ICL evaluation using a 2D GMM. The percentage of correctly assigned number of components from ICL evaluation increases with increasing electron dose when measurements from the 40-170 mrad detector (orange curve) and a combination of two images (yellow curve) are used. However, despite the high amount of electrons collected in the low angle detector regions, the datasets corresponding to the 21-40 mrad detector only is unable to retrieve the correct number of components. This is because of the high contribution of coherent scattering in this LAADF STEM setting that results in a non-monotonic increase of the scattering cross-sections as a function of thickness. As a result, it is impossible to cluster the data correctly. However, despite the unreliable measurement obtained from this detector region only, this set of scattering cross-sections helps the classification process, as the accuracy of model order selection is consistently higher than that of the single ADF STEM measurement. These results indicate the potential benefit of analysing multiple ADF STEM images for a mono-atomic nanostructure when low electron dose settings are required.

Subsequently, also the percentage of correctly counted atomic columns and the root-mean-square error (RMSE) for the atom-counting results can be evaluated. This evaluation was done for the nanoparticle shown in Fig. 2. Also here, 100 noise realisations were generated for the pair of scattering cross-section values at each of the different incident electron doses. The results are presented in Fig. 5. The fraction of correctly counted atomic columns is computed for the scattering cross-sections resulting from the single detectors (blue and orange curves). Those fractions are compared to the fraction for the combination of the scattering cross-section values resulting from the two detectors. As expected, the percentage of correctly counted atomic columns increases with increasing incident electron dose for all sets of measurements. Similarly, the RMSE decreases with increasing dose. In particular, the combination of two images yields a higher percentage of correctly counted atomic columns and a lower RMSE. The key factors for obtaining accurate atom-counting results from the combination of the scattering cross-sections from two detector regions is both the higher percentage of correctly determining the model order using the ICL and the accurate estimation of the locations of the components in the GMM. This result implies that the statistics-based atom-counting method using the 2D GMM provides a dose-efficient analysis.

5. Prospects for heterogeneous nanomaterials

In many cases, the observations obtained from a single ADF STEM image yield accurate and precise estimations for atom counting in mono-atomic nanostructures [5, 12]. In the previous paragraph, it was shown that the atom counting reliability can be further improved when analysing a combination of two images. However, it should be noted that the benefit of combining two images is limited for mono-atomic nanostructures, as a single image may already be sufficient for most cases. The most significant advantage of using two images is therefore expected when analysing heterogeneous nanostructures where information obtained from a single ADF STEM image would lead to an ambiguous classification of the components in the GMM. Indeed, for mixed columns, all type of elements will

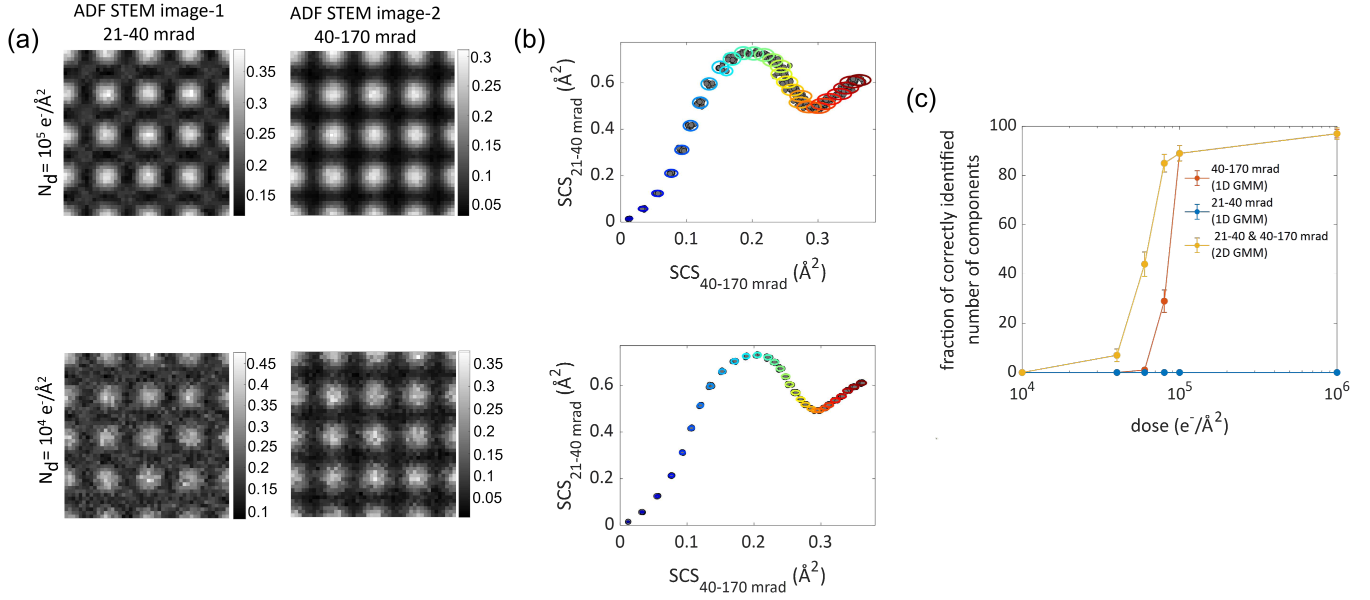

Figure 4: (a) Simulated ADF STEM images for a Ni unit cell in [100] orientation of 30 atoms thick including Poisson noise accounting for an electron dose of $10^5 e^-/\text{Å}^2$ (above) and $10^4 e^-/\text{Å}^2$ (bottom). (b) Distribution of the scattering cross-sections obtained from the combination of two images for an electron dose of $10^5 e^-/\text{Å}^2$ (above) and $10^4 e^-/\text{Å}^2$ (bottom). (c) Fraction of correctly identified number of components (G = 30) as a function of the incident electron dose based on the scattering cross-sections corresponding to detector collection regions from 21-40 mrad (blue curves), 40-170 mrad (orange curves) and from the combination of two images. A set of 100 noise realisations was generated for each STEM image.

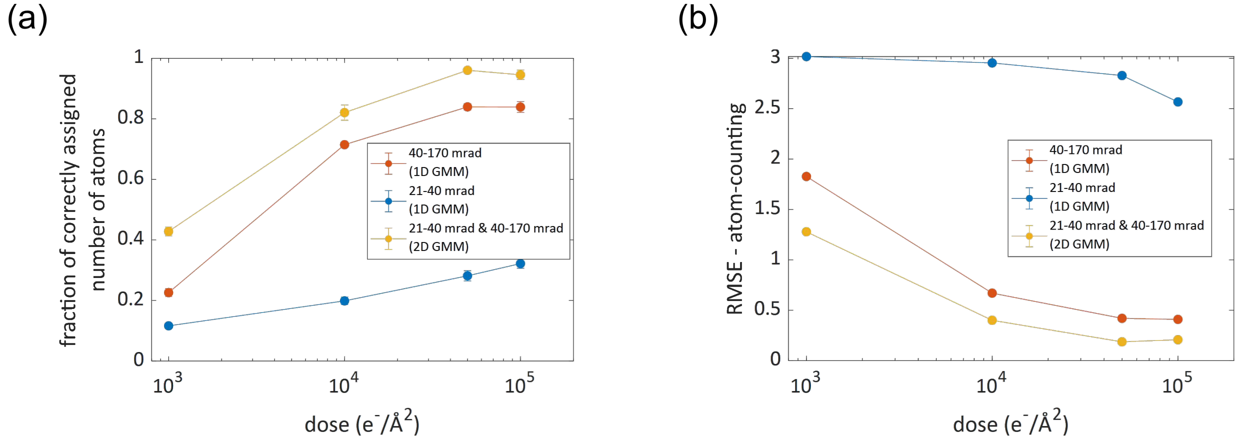

Figure 5: (a) Fraction of correctly assigned number of atoms with the 1D GMM from Image-1 (blue), Image-2 (orange), and the 2D GMM estimation from the combination of the two images (yellow) as a function of the incident electron dose. (b) The root-mean-square error for the estimated atom-counting results as a function of the incident electron dose.

contribute differently to the scattering cross-sections thus significantly complicating the quantitative interpretation as compared to monotype nanostructures. In practice this means that a plenitude of combinations of mixed element atomic columns will lead to similar scattering cross-section values. To unravel both the type and number of atoms, additional images are indispensable. Therefore, we will here focus on the benefits of combining two images and using the 2D GMM methodology to count the number of atoms for different types of elements in a heterogeneous nanostructure.

We evaluate the performance of this approach under different incident electron dose conditions, using an exploratory example of a bulk nanostructure containing two types of atomic columns, i.e. pure Ag (Z = 47) and Au (Z = 79), with varying thicknesses ranging from 1 to 15 atoms. The annular detector collection regions used to reconstruct the ADF STEM images are chosen as 21-43 mrad and 43-170 mrad since they have been derived as optimal for this type of structure in [22]. In Fig. 6(a), the distribution of scattering cross-sections obtained from two ADF STEM images is presented for an incident electron dose of $10^4 e^-/\text{Å}^2$. The scattering cross-section measurements corresponding to Au atomic columns are shown in yellow, while the Ag atomic columns are shown in grey. Additionally, the probability distribution functions of the

scattering cross-sections corresponding to the 30 different types of pure Ag and Au atomic columns are shown on both the x- and y-axis. The probability distributions clearly show that the scattering cross-sections of a significant number of Ag and Au atomic columns overlap on both axes. This explains the difficulty of accurately identifying the number of different types of atoms in a heterogeneous nanostructure using only a single ADF STEM image since the number of components would be underestimated. From the scatter plot in Fig. 6(a) with the scattering cross-sections of the second detector plotted as a function of the scattering cross-sections of the first detector, it is clear that the overlap of scattering cross-sections is reduced allowing for a unique classification of the atomic columns with the same type and number of atoms in 2D. In Fig. 6(b), the estimated 2D Gaussian mixture model for the simulated scattering cross-sections of Fig. 6(a) with an incident electron dose of $10^4 e^-/\text{Å}^2$ is presented.

Using 100 noise realisations for the scattering cross-sections at different dose values, the percentage of correctly identified number of components using the ICL criterion is evaluated. In Fig. 6(c), this percentage is shown for the single scattering cross-section datasets and the combination of the scattering cross-sections from the two detectors. The blue and orange curves obtained from the 1D analyses illustrate that the correct number of components cannot be obtained. In contrast, the yellow curve obtained from the 2D analysis provides a significantly higher percentage when the incident electron dose is larger than $10^3 e^-/\text{Å}^2$.

The benefit of the 2D Gaussian mixture model can also be proven based on a set of scattering cross-sections corresponding to a Au@Ag core-shell nanoparticle. For this type of structure, the total number of atoms and the number of Ag and Au atoms in the column varies. For this example, the thickest columns contain 10 atoms. In Fig. 6(d), the scattering cross-sections are shown in a scatter plot for an incident electron dose of $2 \cdot 10^4 e^-/\text{Å}^2$. The scattering cross-sections of the pure Ag columns, from the shell, are indicated by the grey dots, whereas the scattering cross-sections of the mixed columns, containing both Au and Ag atoms, are indicated in turquoise. The optimal angles for the two detectors are 21-27 mrad and 27-170 mrad as derived in [22]. The corresponding estimated 2D Gaussian mixture model is presented in Fig. 6(e). From the analysis in Fig. 6(f), it is clear that the 2D Gaussian mixture model helps to cluster the atomic columns with the same composition in a correct manner. In general, for both examples in this section, the combination of the two datasets from the two detectors enables the differentiation between the overlapping measurements along one axis and as such a correct assessment of the number of components in the GMM.

6. Conclusions

In this paper, we presented the extension of a 1D GMM to a 2D GMM to analyse a two-dimensional dataset of scattering cross-section values resulting from two ADF STEM images with non-overlapping collection angles. In order to obtain reliable estimates for the parameters of the 2D GMM, the emEM algorithm is used. This algorithm consists of several short and long runs (in terms of convergence tolerance levels) of the traditional expectation maximisation algorithm. This is an elegant workaround for the high dependence of the EM algorithm on the starting values, which becomes more complex in 2D.

Although the atom-counting method from a single ADF STEM image proposed in [4] provides reliable results for monotype crystalline nanostructures, some limitations associated with the imaging and statistical conditions have been reported [5]. The number of atomic columns available in the observed STEM image, the number of components in the estimated probability distribution, and the width of the components of the probability distribution, directly affect the accuracy and precision with which the number of atoms in a particular atomic column can be estimated. Using a detailed simulation study, it is shown that these criteria are less strict for our extended method. The additional information originating from a second detector regime improves the performance toward lower doses and for smaller nanostructures.

Although the two-dimensional Gaussian mixture model (2D GMM) methodology has advantages for analysing homogeneous nanostructures, our results indicate that the most significant benefit of this methodology is obtained for the identification of atomic columns of multi-element nanostructures. Since the scattering cross-section measurements of different elements and thicknesses would coincide, it is challenging to distinguish even how many different types of atomic columns exist in the structure by using a single STEM image. In such cases, the differences in scattering behaviour from low and high angle detector regions would be beneficial and it has been shown that the large amount of electrons collected in LAADF STEM images would be helpful to unscramble the information that can not be obtained using a single HAADF STEM image [22]. It is shown that the 2D GMM will be a very powerful tool to classify the different types of atomic columns for this purpose.

In conclusion, we have shown that our methodology has potential applications not only for mono-atomic nanostructures but also for the analysis of heterogeneous nanostructures. Furthermore, this methodology can be extended to the analysis of a combination of more than two ADF STEM images obtained from different non-overlapping detector regions which could provide an even more accurate analysis. Thus, our multivariate statistical approach for atom counting has the flexibility to be applied to various scenarios, making it a valuable tool for diverse atom-counting analyses.

Acknowledgements

This work was supported by the European Research Council (Grant 770887 PICOMETRICS to S. Van Aert). This project has received funding from the European Union's Horizon 2020 innovation programme under grant agreement No 823717. The authors acknowledge financial support from the Research Foundation Flanders (FWO, Belgium) through project fundings (G.0267.18N, G.0502.18N, G.0346.21N, and EOS 30489208)

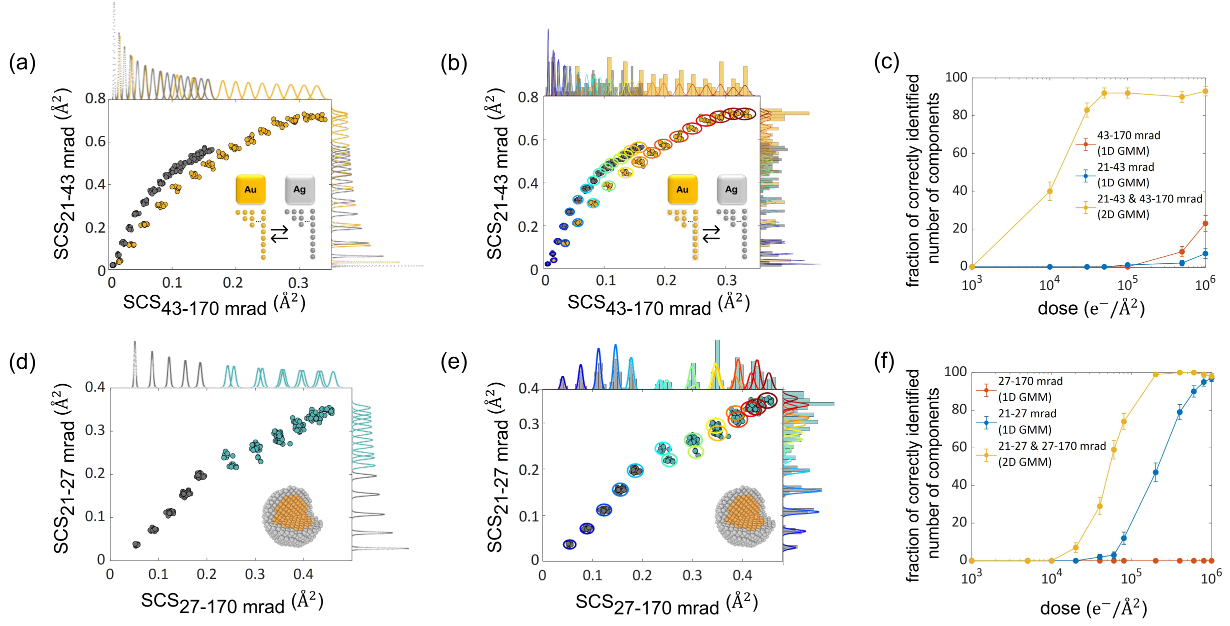

Figure 6: (a) The 2D distribution plot for the simulated pure Au and Ag atomic columns with varying thickness from 1 up to 15 atoms for an electron dose of $10^4 e^-/\text{Å}^2$. (b) Estimated GMM for the scattering cross-sections shown in (a). (c) The fraction of correctly identified number of components ($G = 30$) as a function of dose. (d) The 2D distribution plot for the simulated scattering cross-sections corresponding to a Au@Ag nanoparticle with a maximum thickness of 10 atoms for an electron dose of $2 \cdot 10^4 e^-/\text{Å}^2$. (e) Estimated GMM for the scattering cross-sections shown in (d). (f) The fraction of correctly identified number of components ($G = 16$) as a function of dose.

and a postdoctoral grant to A. De Backer. S. Van Aert acknowledges funding from the University of Antwerp Research fund (BOF).

Appendix A. Probability of error and optimal setting for ADF STEM images

To obtain reliable atom-counting results, one can predict the optimal collection angles of the annular detector. For this purpose, the probability of error was introduced and applied [22]. Using statistical detection theory, the atom-counting problem is then formulated as a statistical hypothesis test, where each hypothesis corresponds to a specific number (and type) of atoms in an atomic column. The probability of error corresponds to the probability to choose the wrong hypothesis. To compute the probability of error, realistic 4D STEM simulations of the Ni nanoparticle are used from which multiple 2D STEM images were generated with varying inner and outer detector angles.The probability of error is computed based on the scattering cross-section values extracted from these virtual 2D STEM images. The result of the probability of error for an incident electron dose of $10^3 e^-/\text{Å}^2$ is illustrated in Fig. Appendix A.1. The probability of error is here computed for two non-overlapping detectors with a shared angle x which is the outer angle for the inner detector (21-x mrad - red detector) and the inner angle for the outer detector (x-170 mrad - blue detector). The optimal settings for the combination of two non-overlapping detectors correspond to 21-40 mrad and 40-170 mrad, a indicated by the minimum of the yellow curve.

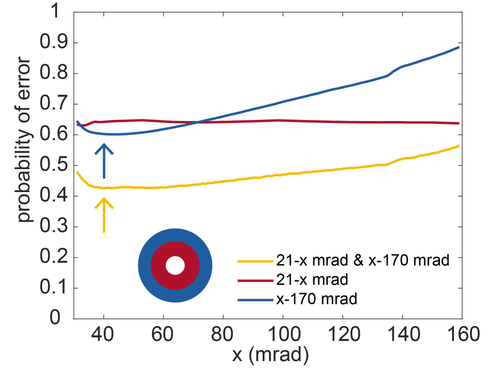

Figure Appendix A.1: Probability of error as a function of the outer angle of a single ADF detector with fixed inner angle (red), the inner angle of a single ADF detector with a fixed outer angle (blue), and the common angle x for two non-overlapping detectors (yellow) for an incident electron dose of $10^3 e^-/\text{Å}^2$

References

[1] P. D. Nellist, S. J. Pennycook, The Principles and Interpretation of Annular Dark-Field Z-Contrast Imaging, Advances in Imaging and Electron Physics 113 (2000) 147–203.

[2] N. Shibata, Y. Kohno, S. D. Findlay, H. Sawada, Y. Kondo, Y. Ikuhara, New area detector for atomic-resolution scanning transmission electron microscopy, Journal of Electron Microscopy 59 (2010) 473–479.

[3] J. M. LeBeau, S. D. Findlay, L. J. Allen, S. Stemmer, Standardless Atom Counting in Scanning Transmission Electron Microscopy, Nano Letters 10 (2010) 4405–4408.

[4] S. Van Aert, K. J. Batenburg, M. D. Rossell, R. Erni, G. Van Tendeloo, Three-dimensional atomic imaging of crystalline nanoparticles, Nature 470 (2011) 374–377.

[5] A. De Backer, G. T. Martinez, A. Rosenauer, S. Van Aert, Atom counting in HAADF STEM using a statistical model-based approach: Methodol-

ogy, possibilities, and inherent limitations, Ultramicroscopy 134 (2013) 23–33.

[6] A. De wael, A. De Backer, L. Jones, P. Nellist, S. Van Aert, Hybrid statistics-simulations based method for atom-counting from ADF STEM images, Ultramicroscopy 177 (2017) 69–77.

[7] S. Bals, M. Casavola, M. A. van Huis, S. Van Aert, K. J. Batenburg, G. Van Tendeloo, D. Vanmaekelbergh, Three-Dimensional Atomic Imaging of Colloidal Core-Shell Nanocrystals, Nano Letters 11 (2011) 3420–3424.

[8] L. Jones, K. E. MacArthur, V. T. Fauske, A. T. J. van Helvoort, P. D. Nellist, Rapid Estimation of Catalyst Nanoparticle Morphology and Atomic-Coordination by High-Resolution Z-Contrast Electron Microscopy, Nano Letters 14 (2014) 6336–6341.

[9] A. De Backer, L. Jones, I. Lobato, T. Altantzis, B. Goris, P. D. Nellist, S. Bals, S. Van Aert, Three-dimensional atomic models from a single projection using Z-contrast imaging: verification by electron tomography and opportunities, Nanoscale 9 (2017) 8791–8798.

[10] A. De Backer, S. Bals, S. Van Aert, A decade of atom-counting in STEM: From the first results toward reliable 3D atomic models from a single projection, Ultramicroscopy 247 (2023) 113702.

[11] R. Erni, H. Heinrich, G. Kostorz, Quantitative characterisation of chemical inhomogeneities in Al-Ag using high-resolution Z-contrast STEM, Ultramicroscopy 94 (2003) 125–133.

[12] S. Van Aert, A. De Backer, G. T. Martinez, B. Goris, S. Bals, G. Van Tendeloo, Procedure to count atoms with trustworthy single-atom sensitivity, Physical Review B 87 (2013).

[13] S. Van Aert, J. Verbeeck, R. Erni, S. Bals, M. Luysberg, D. V. Dyck, G. V. Tendeloo, Quantitative atomic resolution mapping using high-angle annular dark field scanning transmission electron microscopy, Ultramicroscopy 109 (2009) 1236–1244.

[14] H. E, K. E. MacArthur, T. J. Pennycook, E. Okunishi, A. J. D'Alfonso, N. R. Lugg, L. J. Allen, P. D. Nellist, Probe integrated scattering cross sections in the analysis of atomic resolution HAADF STEM images, Ultramicroscopy 133 (2013) 109–119.

[15] G. T. Martinez, A. Rosenauer, A. De Backer, J. Verbeeck, S. Van Aert, Quantitative composition determination at the atomic level using model-based high-angle annular dark field scanning transmission electron microscopy, Ultramicroscopy 137 (2014) 12–19.

[16] K. E. MacArthur, A. J. D'Alfonso, D. Ozkaya, L. J. Allen, P. D. Nellist, Optimal ADF STEM imaging parameters for tilt-robust image quantification, Ultramicroscopy 156 (2015) 1–8.

[17] A. Rosenauer, T. Mehrtens, K. Müller, K. Gries, M. Schowalter, P. Venkata Satyam, S. Bley, C. Tessarek, D. Hommel, K. Sebald, M. Seyfried, J. Gutowski, A. Avramescu, K. Engl, S. Lutgen, Composition mapping in InGaN by scanning transmission electron microscopy, Ultramicroscopy 111 (2011) 1316–1327.

[18] A. De Backer, A. De wael, J. Gonnissen, S. Van Aert, Optimal experimental design for nano-particle atom-counting from high-resolution stem images, Ultramicroscopy 151 (2015) 46–55.

[19] A. De Backer, G. Martinez, K. MacArthur, L. Jones, A. Béché, P. Nellist, S. Van Aert, Dose limited reliability of quantitative annular dark field scanning transmission electron microscopy for nano-particle atom-counting, Ultramicroscopy 151 (2015) 56–61.

[20] P. Hartel, H. Rose, C. Dinges, Conditions and reasons for incoherent imaging in STEM, Ultramicroscopy 63 (1996) 93–114.

[21] S. Pennycook, L. Boatner, Chemically sensitive structure-imaging with a scanning transmission electron microscope, Nature 336 (1988) 565 – 567.

[22] D. G. Sentürk, A. De Backer, T. Friedrich, S. Van Aert, Optimal experiment design for element specific atom counting using multiple annular dark field scanning transmission electron microscopy detectors, Ultramicroscopy 242 (2022) 113626.

[23] C. Ophus, Four-Dimensional Scanning Transmission Electron Microscopy (4d-stem): From Scanning Nanodiffraction to Ptychography and Beyond, Microscopy and Microanalysis 25 (2019) 563–582.

[24] G. McLachlan, D. Peel, Finite Mixture Models, Wiley series in probability and statistics. John Wiley and Sons, inc., 2000.

[25] S. Van Aert, A. De Backer, L. Jones, G. T. Martinez, A. Béché, P. D. Nellist, Control of Knock-On Damage for 3D Atomic Scale Quantification of Nanostructures: Making Every Electron Count in Scanning Transmission Electron Microscopy, Phys. Rev. Lett. 122 (2019) 066101.

[26] V. Hasselblad, Estimation of Finite Mixtures of Distributions from the Exponential Family, Journal of the American Statistical Association 64 (1969) 1459–1471.

[27] N. E. Day, Estimating the Components of a Mixture of Normal Distributions, Biometrika 56 (1969) 463–474.

[28] J. H. Wolfe, Pattern clustering by multivariate mixture analysis, Multivariate Behavioral Research 5 (1970) 329–350.

[29] C. Biernacki, G. Celeux, G. Govaert, Choosing starting values for the EM algorithm for getting the highest likelihood in multivariate gaussian mixture models, Computational Statistics & Data Analysis 41 (2003) 561–575.

[30] S. Michael, V. Melnykov, An effective strategy for initializing the EM algorithm in finite mixture models, Advances in Data Analysis and Classification 10 (2016) 563–583.

[31] E. Celebi, Partitional Clustering, Encyclopedia of Machine Learning and Data Mining, 2017.

[32] B. Panić, J. Klemenc, M. Nagode, Improved initialization of the EM algorithm for mixture model parameter estimation, Mathematics 8 (2020) 373.

[33] B. M. Shireman E, Steinley D, Examining the effect of initialization strategies on the performance of gaussian mixture modeling, Behav Res Methods. 49(1) (2017) 282–293.

[34] C. Biernacki, G. Celeux, G. Govaert, Assessing a mixture model for clustering with the integrated completed likelihood, IEEE Transactions on Pattern Analysis and Machine Intelligence 22 (2000) 719–725.

[35] I. Lobato, D. Van Dyck, MULTEM: A new multislice program to perform accurate and fast electron diffraction and imaging simulation using Graphics Processing Units with CUDA, Ultramicroscopy 156 (2015) 9–17.

[36] A. Beyer, F. F. Krause, H. L. Robert, S. Firoozabadi, T. Grieb, P. Kükelhan, D. Heimes, M. Schowalter, K. Müller-Caspary, A. Rosenauer, K. Volz, Influence of plasmon excitations on atomic-resolution quantitative 4d scanning transmission electron microscopy, Sci Rep 10 (2020) 17890.

[37] A. De Backer, K. H. W. van den Bos, W. Van den Broek, J. Sijbers, S. Van Aert, StatSTEM: An efficient approach for accurate and precise model-based quantification of atomic resolution electron microscopy images, Ultramicroscopy 171 (2016) 104–116.